Hindawi Publishing Corporation
Mathematical Problems in Engineering
Volume 2016, Article ID 7896035, 13 pages
http://dx.doi.org/10.1155/2016/7896035

Research Article

Grinding Parameter Optimization of Ultrasound-Aided Electrolytic in Process Dressing for Finishing Nanocomposite Ceramics

Fan Chen, Bo Zhao, Xiao-feng Jia, Chong-yang Zhao, and Jing-lin Tong

School of Mechanics and Power Engineering, Henan Polytechnic University, Jiaozuo 454003, China

Correspondence should be addressed to Bo Zhao; zhaob@hpu.edu.cn

Received 9 April 2016; Revised 26 June 2016; Accepted 15 August 2016

Academic Editor: Yuri Vladimirovich Mikhlin

In order to achieve the precision and efficient processing of nanocomposite ceramics, the ultrasound-aided electrolytic in process dressing method was proposed. But how to realize grinding parameter optimization, that is, the maximum processing efficiency, on the premise of the assurance of best workpiece quality is a problem that needs to be solved urgently. Firstly, this research investigated the influence of grinding parameters on material removal rate and critical ductile depth, and their mathematic models based on the existing models were developed to simulate the material removal process. Then, on the basis of parameter sensitivity analysis based on partial derivative, the sensitivity models of material removal rates on grinding parameter were established and computed quantitatively by MATLAB, and the key grinding parameter for optimal grinding process was found. Finally, the theoretical analyses were verified by experiments: the material removal rate increases with the increase of grinding parameters, including grinding depth (a_p), axial feeding speed (f_a), workpiece speed (V_w), and wheel speed (V_s); the parameter sensitivity of material removal rate was in a descending order as $a_p > f_a > V_w > V_s$; the most sensitive parameter (a_p) was optimized and it was found that the better machining result has been obtained when a_p was about 3.73 μm.

1. Introduction

Nanocomposite ceramics is composite that at least one of its phases is at nanoscale size, and this substance has revealed that it is suitable as an alternative to overcome limitations of microstructure and being monolithic, while posing preparation challenges related to the control of elemental composition and stoichiometry in the nanocluster phase. They have been used for getting better physical properties, such as a high strength at high temperatures, show low thermal expansion, have good wear resistance, and are chemically inert, which are superior to conventional microscale composites and can be synthesized using simple and inexpensive technique [1]. As a result, this material has become a popular research topic in military, aerospace, precise instruments, and machine-tool industries, but the applications for it have been impeded by high finishing costs and by damage caused during the finishing process due to the material's brittleness, poor uniformity, low reliability, and low malleability [2]. Therefore, developing cost-effective nanocomposites ceramic machining technique can significantly broaden its possible applications. To solve the problem, researchers have examined many ultraprecise machining methods, such as prestressed machining, ELID grinding, magnetic abrasive polishing, and ultrasonic vibration machining [3–7]. Currently, ELID grinding and ultrasonic vibration-aided grinding are considered to be fairly mature methods. ELID grinding can obviously increase grinding efficiency, but in general the influence degree is rather limited. However, ultrasonic vibration-aided grinding can improve surface quality and grinding efficiency, but its abrasive grains cannot retain sharpness during grinding. So we proposed the ultrasound-aided electrolytic in process dressing (U-ELID grinding) to combine the benefits of these two methods [8].

A common problem for grinding is that the choice of process plan still counts on traditional trial cutting and

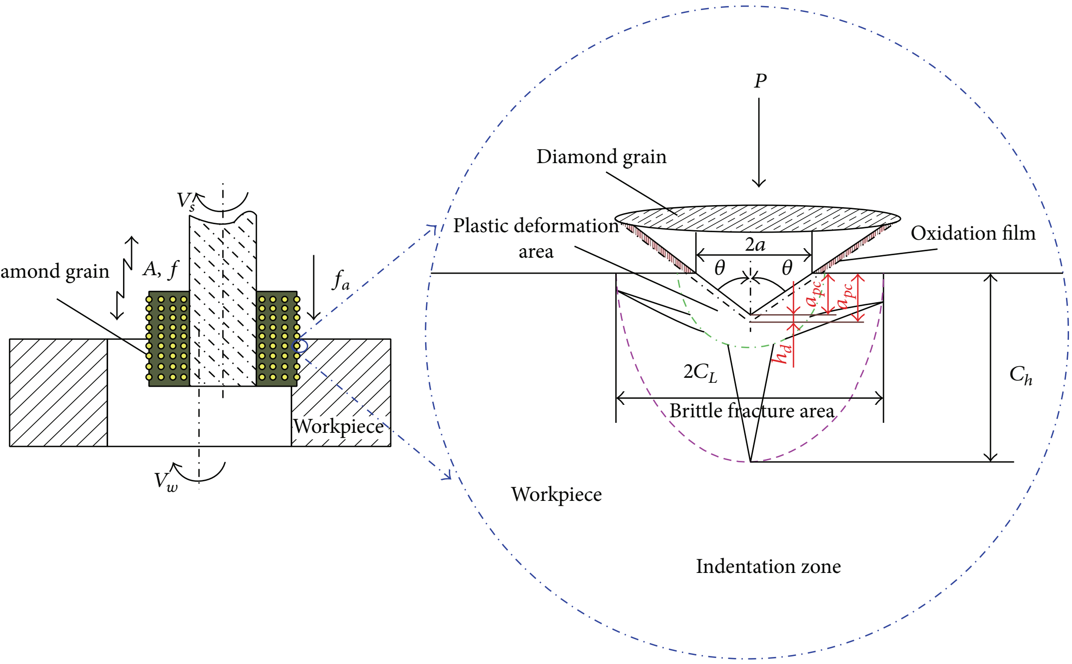

FIGURE 1: Motion state of a grain on diamond wheel in U-ELID grinding.

empirical method, which heavily rely on the field engineer's experiences, and is poor in processing efficiency and flexibility [9]. The U-ELID grinding system is complex because of interdependence of ultrasonic vibration and ELID grinding, the processing can be affected by many conditions, and the processing parameters have difficulty realizing real-time monitoring precisely. So the manufacturer is always puzzled how to choose a best process plan of grinding process. How to realize the overall improvement of grinding quality, the maximization of economic benefits, and the biggest use of machining capacity, that is, the maximum processing efficiency being realized on the premise of the assurance of best workpiece quality, is a problem that cannot wait to be solved [10]. Therefore, the material removal rate and critical ductile depth models for the U-ELID grinding were developed based on the principle of grinding and the existing material removal models, and the effects degree models of various grinding parameters were obtained by partial derivative. Finally the experiments have proved the reliability of these models, and the rational process parameters have been determined, which can be used to optimize other parameters and guide machining in the U-ELID grinding for nanocomposite ceramics.

2. Theoretical Analysis about Grinding Parameter Optimization

In the U-ELID grinding, the motion state of a grain on diamond wheel and the interaction process of a grain and workpiece were shown in Figure 1. Parameter optimization is to realize the maximum processing efficiency on the premise of the assurance of best workpiece quality, which should mainly include two parts: machining efficiency and machining quality. As the critical ductile depth has a greater impact on both material removal rate and machining surface quality, it was necessary to theoretically analyze it in detail when optimizing grinding parameter.

2.1. Critical Ductile Depth. From Figure 1, we can see that the interaction process between a grain and workpiece is similar to an indentation experiment. So, assuming the workpiece material is rigid-plastic, the relationship between contact force (P) and feature size ($2a$) on the indentation experiment can be expressed as follows [11]:

$$P = \xi \cdot H_v \cdot a^2. \tag{1}$$

In Figure 1, the material damage is controlled by plastic deformation when the external load (P) is less than the critical ductile depth (P_c), and at the moment the ductile mode is the main material removal method, as shown in the region which was bounded by green circle. However, when the load increases more than the critical ductile depth, more portions of material were removed by crack propagation. Moreover, Bifano et al. [12] found that there is a radial crack at the bottom of the plastic deformation zone, and it expands in reach; during unloading, under the combined action of local plastic deformation and the stress field, the transverse crack appears and extends forward until it reaches the workpiece surface to form the partial peeling block when satisfying the transversal crack expanding condition, as shown the region which was bounded by green circle and carmine circle. Wilshaw et al. [13] also described that having an external load that is higher than the critical ductile depth can lead to crack propagation and brittle fractures, and the critical ductile depth can be expressed as follows:

$$P_c = \lambda_0 K_{IC} \left(\frac{K_{IC}}{H_v} \right)^3 . \tag{2}$$

According to the grinding working principle, we learned the vertical load is determined by indentation depth or grinding depth. From Figure 1, the actual grinding depth can be written as

$$a = a'_{pc} \cdot \tan\theta. \tag{3}$$

In an indentation experiment there are all the contact surfaces of diamond indenter in close contact with specimen, but in machining there are only about half. So the critical indentation depth or the critical ductile depth of single diamond grit can be obtained.

$$a'_{pc} = \frac{K_{IC}^2}{H_v^2 \tan\theta} \sqrt{\frac{2\lambda_0}{\xi}}. \tag{4}$$

Equation (4) was obtained in the static condition. In dynamic grinding, it was subjected to the complicated intermitted machining and there was a great impact when the grit hit the workpiece, so the wearing surface differed in shape and size compared with that in the static condition, and (4) cannot reflect the real response. Since the dynamic characteristic is influenced by many factors in the U-ELID grinding such as ultrasonic and grinding parameters, in order to simplify the analytical process, the specific impacts of dynamic parameters on dynamic fracture toughness have not been further analyzed, but the total impact was considered by introducing one coefficient (K_d). So, in the dynamic grinding, (4) can be rewritten as follows:

$$a'_{pc} = K_d \cdot \frac{K_{IC}^2}{H_v^2 \tan\theta} \sqrt{\frac{2\lambda_0}{\xi}}. \tag{5}$$

ELID, namely, electrolytic in-process dressing, can ensure in-process diamond wheel dressing by the combined effect of both the wheel wear and electrolysis, which not only relates to grinding wheel surface topography and grinding depth, but also influences the shape accuracy and the surface quality of workpiece [14]. Therefore, when the critical ductile depth was analyzed, it was necessary to consider the combined effect in ELID grinding. Because the combined effect can reach a dynamic equilibrium, the wheel mass loss can be represented by the electrolyte content. Using the principle of Faraday's law, through simple integration, the electrolyte content (V_v) can be written:

$$V_v = \eta \frac{M \cdot I \cdot t}{z \cdot F \cdot \rho}. \tag{6}$$

Oxidation film on grinding wheel surface was formed by the product produced in the electrolysis and plays an important role in the ELID grinding [15]. The thickness of oxidation film (h_d) can be expressed as follows [8]:

$$h_d = \frac{V_v}{A_a} = \eta \frac{M \cdot I \cdot t}{z \cdot F \cdot \rho \cdot A_a} = \frac{\eta \cdot M \cdot t \cdot U \cdot A_c}{z \cdot F \cdot \rho \cdot A_a \cdot R}. \tag{7}$$

From Figure 1, we could find the relationship between grinding depth and thickness of oxidation film. Based on these formulas, the actual critical ductile depth can be expressed as follows:

$$\begin{aligned} a'_{pc} &= a_{pc} - h_d \\ &= K_d \cdot \frac{K_{IC}^2}{H_v^2 \cdot \tan\theta} \sqrt{\frac{2\lambda_0}{\xi}} - \frac{\eta \cdot M \cdot t \cdot U \cdot A_c}{z \cdot F \cdot \rho \cdot A_a \cdot R}. \end{aligned} \tag{8}$$

Similarly, the actual grinding depth can be written as

$$a'_p = a_p - \frac{\eta \cdot M \cdot t \cdot U \cdot A_c}{z \cdot F \cdot \rho \cdot A_a \cdot R}. \tag{9}$$

2.2. Material Removal Rate. In summary, there were two kinds of material removal: ductile mode and brittle fracture mode [16]. From Figure 1, according to the reference materials, the material removal rate can be expressed as [8].

$$M_r = N_d \cdot V \cdot S = \begin{cases} C_s \cdot \tan\theta \cdot f_a \cdot a'^2_p \cdot \sqrt{a'_p \cdot d_{se}} \cdot \left(\dfrac{V_s}{V_w} \right)^{C_g} \cdot \left[\tan^{-1} \left(\dfrac{V_w}{V_s} \sqrt{\dfrac{a'_p}{d_{se}}} \right) \right]^{C_g} \cdot \sqrt{V_x^2 + V_y^2} & a'_p < a'_{pc} \\ C_s \cdot \dfrac{\pi}{2} \cdot C_L \cdot C_h \cdot f_a \cdot \sqrt{a'_p \cdot d_{se}} \cdot \left(\dfrac{V_s}{V_w} \right)^{C_g} \cdot \left[\tan^{-1} \left(\dfrac{V_w}{V_s} \sqrt{\dfrac{a'_p}{d_{se}}} \right) \right]^{C_g} \cdot \sqrt{V_x^2 + V_y^2} & a'_p > a'_{pc}. \end{cases} \tag{10}$$

Suppose the diamond grit was adequate stiff and the work material was an isotropic composite during machining. The movement track of one diamond grit on a part of workpiece was established in the U-ELID grinding, as shown in Figure 2. The cutting trace of single diamond grit in U-EILD grinding was marked in red curve and its velocity equation of the diamond grit in U-EILD grinding can be represented as follows:

$$\begin{aligned} V_x &= V_s - V_w, \\ V_y &= A \cdot \omega \cdot \cos(\omega \cdot t + \varphi) + f_a. \end{aligned} \tag{11}$$

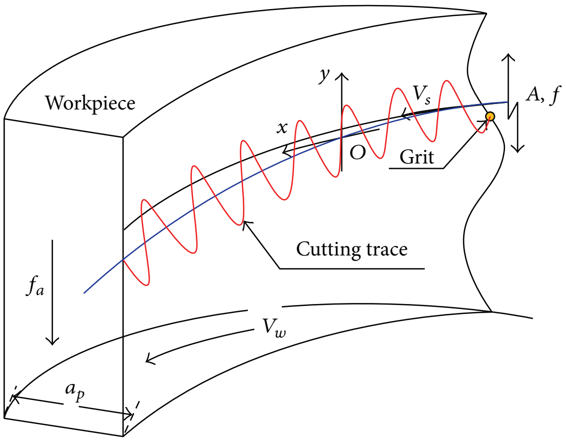

Figure 2: Cutting trace of a diamond grit in U-EILD grinding.

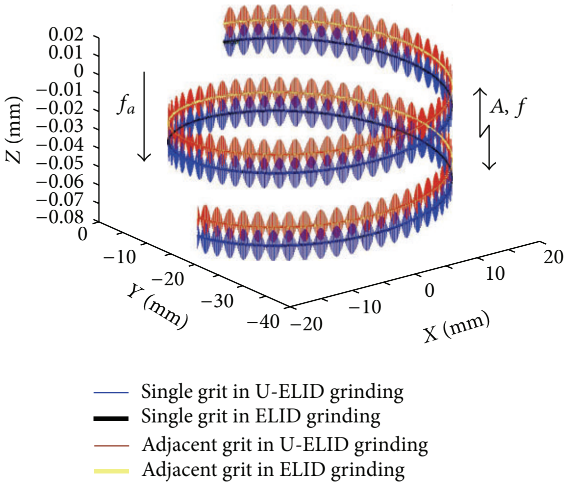

Figure 3: Cutting trace of single abrasive grains in axial direction with ultrasonic vibration.

In the U-ELID grinding, geometrically generating interaction between grits and workpiece surface was different from that in the ordinary ELID grinding. This was because the effect by the axial ultrasonic vibration of grinding wheel and the interaction of adjacent grains had a proportionately larger impact on it. According to movement equation under U-ELID grinding and ELID grinding, using MATLAB, Figure 3 shows the difference.

From Figure 3, the movement track was a spiral line and not to interfere with another in the normal ELID grinding, but it was a sinusoid along the spiral and intervened with that of other adjacent grits in the U-ELID grinding. In the U-ELID grinding, many sinusoids overlapped seriously and formed the interlaced situation, increasing the removal volume of workpiece, which was the fundamental reason for the ultrasonic grinding being able to greatly increase the machining efficiency. Therefore, the weight coefficient (K_m) was introduced in order to consider the influence of the ultrasonic vibration, and the material removal rate can be rewritten as

$$\begin{aligned} M_r &= K_m \cdot N_d \cdot V \cdot S \\ &= \begin{cases} K_m \cdot C_s \cdot \tan\theta \cdot f_a \cdot a_p'^2 \cdot \sqrt{a_p' \cdot d_{se}} \cdot \left(\dfrac{V_s}{V_w}\right)^{C_g} \cdot \left[\tan^{-1}\left(\dfrac{V_w}{V_s}\sqrt{\dfrac{a_p'}{d_{se}}}\right)\right]^{C_g} \cdot \sqrt{\left(V_s - V_w\right)^2 + \left[A \cdot \omega \cdot \cos\left(\omega \cdot \dfrac{\sqrt{a_p' \cdot d_{se}}}{V_s} + \varphi\right) + f_a\right]^2} & a_p' < a_{pc}' \\ K_m \cdot C_s \cdot \dfrac{\pi}{2} \cdot C_L \cdot C_h \cdot f_a \cdot \sqrt{a_p' \cdot d_{se}} \cdot \left(\dfrac{V_s}{V_w}\right)^{C_g} \cdot \left[\tan^{-1}\left(\dfrac{V_w}{V_s}\sqrt{\dfrac{a_p'}{d_{se}}}\right)\right]^{C_g} \cdot \sqrt{\left(V_s - V_w\right)^2 + \left[A \cdot \omega \cdot \cos\left(\omega \cdot \dfrac{\sqrt{a_p' \cdot d_{se}}}{V_s} + \varphi\right) + f_a\right]^2} & a_p' > a_{pc}', \end{cases} \end{aligned} \tag{12}$$

where $a_p' = a_p - (\eta \cdot M \cdot t \cdot U \cdot A_c)/(z \cdot F \cdot \rho \cdot A_a \cdot R)$.

From (12), in the U-ELID grinding, the material removal rate was determined by ultrasonic parameters, ELID electrical parameters, and grinding parameters. Among them, ultrasonic parameters and ELID electrical parameters had difficulty in realizing real-time control during processing. So, in order to verify the reliability of the model, these modes were quantitatively analyzed by MATLAB under different grinding parameters, and the related parameters were shown in Table 1.

After calculation, the removal model changed from ductile removal to brittle fracture when grinding depth was about 3.73 μm. Due to the fact that the brittle fracture model removes materials in the form of large size and irregular shape, the machining surface quality was deteriorated seriously. So it can be predicted that the surface quality was good only when the grinding depth was less than 3.73 μm. Moreover, the variation of material removal rate with grinding parameters was shown in Figure 4.

As can be seen from Figure 4, the material removal rate increases overall within certain boundaries; it increases as grinding depth, axial feed velocity, and wheel speed increase. However, the workpiece speed has no obvious influence, which suggests that further increasing the workpiece speed will not effectively increase the material removal rate and need to consider the grinding quality to determine the scope of workpiece speed for parameter prioritizing.

2.3. Models of Grinding Parameter Sensitivity to Material Removal Rate.

Parameter sensitivity mathematic models on material removal rate can be determined via parameter sensitivity based on the partial derivative. By seeking the first order partial differential of material removal rate with respect to these grinding parameters, the mathematic models of the parameter sensitivity to material removal rate can be expressed as follows in the U-ELID grinding:

$$\frac{\partial M_r}{\partial V_s} = \begin{cases} a_p'^2 \cdot K_1 \cdot V \cdot f_a \cdot \sqrt{a_p' \cdot d_{se}} \left\{ \dfrac{\left[\tan^{-1}\left(\left(V_w/V_s\right)\sqrt{a_p'/d_{se}}\right)\right]}{V_w} - \dfrac{V_s \cdot \sqrt{a_p' \cdot d_{se}}}{d_{se} \cdot V_s^2 + V_w^2 \cdot a_p'} \right\} \\ \quad + \dfrac{a_p'^2 \cdot V_s \cdot K_1 \cdot f_a \cdot \left[\tan^{-1}\left(\left(V_w/V_s\right)\sqrt{a_p'/d_{se}}\right)\right]}{V_w \cdot V} \cdot \sqrt{a_p' \cdot d_{se}} \\ \quad \cdot \left\{ V_s + V_w + \dfrac{A \cdot \omega^2 \cdot \sqrt{a_p' \cdot d_{se}} \cdot \sin\left(\omega \cdot \sqrt{a_p' \cdot d_{se}}/V_s\right)}{V_s^2} \cdot \left[A \cdot \omega \cdot \cos\left(\omega \cdot \dfrac{\sqrt{a_p' \cdot d_{se}}}{V_s} \right) + f_a \right] \right\} & a_p' < a_{pc}' \\ K_2 \cdot f_a \cdot V \cdot \sqrt{a_p' \cdot d_{se}} \cdot \left\{ \dfrac{\left[\tan^{-1}\left(\left(V_w/V_s\right)\sqrt{a_p'/d_{se}}\right)\right]}{V_w} - \dfrac{V_s \cdot \sqrt{a_p' \cdot d_{se}}}{d_{se} \cdot V_s^2 + V_w^2 \cdot a_p'} \right\} \\ \quad + \dfrac{V_s \cdot K_2 \cdot f_a \cdot \sqrt{a_p' \cdot d_{se}} \cdot \left[\tan^{-1}\left(\left(V_w/V_s\right)\sqrt{a_p'/d_{se}}\right)\right]}{V_w \cdot V} \\ \quad \cdot \left\{ V_s + V_w + \dfrac{A \cdot \omega^2 \cdot \sqrt{a_p' \cdot d_{se}} \cdot \sin\left(\omega \cdot \sqrt{a_p' \cdot d_{se}}/V_s\right)}{V_s^2} \cdot \left[A \cdot \omega \cdot \cos\left(\omega \cdot \dfrac{\sqrt{a_p' \cdot d_{se}}}{V_s} \right) + f_a \right] \right\} & a_p' > a_{pc}', \end{cases}$$

$$\frac{\partial M_r}{\partial V_w} = \begin{cases} \dfrac{a_p'^2 \cdot K_1 \cdot f_a \cdot V_s \cdot \sqrt{a_p' \cdot d_{se}}}{V_w} \cdot \left\{ \dfrac{V \cdot V_s \cdot \sqrt{a_p' \cdot d_{se}}}{d_{se} \cdot V_s^2 + V_w^2 \cdot a_p'} - \dfrac{V \cdot \tan^{-1}\left(\left(V_w/V_s\right)\sqrt{a_p'/d_{se}}\right)}{V_w} + \dfrac{\tan^{-1}\left(\left(V_w/V_s\right)\sqrt{a_p'/d_{se}}\right)}{V \cdot V_w} \right\} & a_p' < a_{pc}' \\ \dfrac{K_2 \cdot f_a \cdot V_s}{V_w} \sqrt{a_p' \cdot d_{se}} \cdot \left\{ \dfrac{V \cdot V_s \cdot \sqrt{a_p' \cdot d_{se}}}{d_{se} \cdot V_s^2 + V_w^2 \cdot a_p'} - \dfrac{V \cdot \left[\tan^{-1}\left(\left(V_w/V_s\right)\sqrt{a_p'/d_{se}}\right)\right]}{V_w} + \dfrac{\tan^{-1}\left(\left(V_w/V_s\right)\sqrt{a_p'/d_{se}}\right)}{V \cdot V_w} \right\} & a_p' > a_{pc}', \end{cases}$$

$$\frac{\partial M_r}{\partial a_p}$$

$$= \begin{cases} \dfrac{1}{2} a_p' \cdot K_1 \cdot V \cdot f_a \cdot \sqrt{a_p' \cdot d_{se}} \left\{ \dfrac{5V_s \cdot \left[\tan^{-1}\left(\left(V_w/V_s\right)\sqrt{a_p'/d_{se}}\right)\right]}{V_w} + \dfrac{V_s^2 \cdot \sqrt{a_p' \cdot d_{se}}}{\left(d_{se} \cdot V_s^2 + V_w^2 \cdot a_p'\right)} \right\} - \dfrac{a_p'^2 \cdot A \cdot \omega^2 \cdot K_1 \cdot f_a}{2V_w \cdot V} \cdot \sqrt{a_p' \cdot d_{se}} \\ \quad \cdot \left[\tan^{-1}\left(\dfrac{V_w}{V_s} \sqrt{\dfrac{a_p'}{d_{se}}} \right) \right] \cdot \left[A \cdot \omega \cdot \cos\left(\omega \cdot \dfrac{\sqrt{a_p' \cdot d_{se}}}{V_s} \right) + f_a \right] \cdot \sin\left(\omega \cdot \dfrac{\sqrt{a_p' \cdot d_{se}}}{V_s} \right) & a_p' < a_{pc}' \\ \dfrac{1}{2} K_2 \cdot f_a \cdot d_{se} \cdot V_s \cdot V \cdot \left\{ \dfrac{\left[\tan^{-1}\left(\left(V_w/V_s\right)\sqrt{a_p'/d_{se}}\right)\right]}{V_w \cdot \sqrt{a_p' \cdot d_{se}}} - \dfrac{V_s}{d_{se} \cdot V_s^2 + V_w^2 \cdot a_p'} \right\} - \dfrac{A \cdot \omega^2 \cdot K_2 \cdot f_a \cdot \left[\tan^{-1}\left(\left(V_w/V_s\right)\sqrt{a_p'/d_{se}}\right)\right] \cdot d_{se}}{2V_w \cdot V} \\ \quad \cdot \left[A \cdot \omega \cdot \cos\left(\omega \cdot \dfrac{\sqrt{a_p' \cdot d_{se}}}{V_s} \right) + f_a \right] \cdot \sin\left(\omega \cdot \dfrac{\sqrt{a_p' \cdot d_{se}}}{V_s} \right) & a_p' > a_{pc}', \end{cases}$$

$$\frac{\partial M_r}{\partial f_a} = \begin{cases} \dfrac{K_1 \cdot a_p'^2 \cdot V_s}{V_w} \cdot \sqrt{a_p' \cdot d_{se}} \cdot \left[\tan^{-1}\left(\dfrac{V_w}{V_s}\sqrt{\dfrac{a_p'}{d_{se}}}\right)\right] \cdot \left\{\dfrac{f_a \cdot \left[2A \cdot \omega \cdot \cos\left(\omega \cdot \sqrt{a_p' \cdot d_{se}}/V_s\right) + f_a\right]}{2V} + V\right\} & a_p' < a_{pc}' \\ \dfrac{K_2 \cdot V_s}{V_w} \cdot \sqrt{a_p' \cdot d_{se}} \cdot \left[\tan^{-1}\left(\dfrac{V_w}{V_s}\sqrt{\dfrac{a_p'}{d_{se}}}\right)\right] \cdot \left\{\dfrac{f_a \cdot \left[2A \cdot \omega \cdot \cos\left(\omega \cdot \sqrt{a_p' \cdot d_{se}}/V_s\right) + f_a\right]}{2V} + V\right\} & a_p' > a_{pc}', \end{cases} \tag{13}$$

where

$$V = \sqrt{\left(V_s - V_w\right)^2 + \left[A \cdot \omega \cdot \cos\left(\omega \cdot \frac{\sqrt{a_p' \cdot d_{se}}}{V_s}\right) + f_a\right]^2}, \tag{14}$$

$$a_p' = a_p - \frac{\eta \cdot M \cdot t \cdot U \cdot A_c}{z \cdot F \cdot \rho \cdot A_a \cdot R},$$

$$K_1 = K_m \cdot C_s \cdot \tan\theta,$$

$$K_2 = K_m \cdot C_s \cdot \frac{\pi}{2} \cdot C_L \cdot C_h.$$

These mathematical models of parameter sensitivity to material removal rate were calculated by MATLAB, and the related parameters were shown in Table 1. The change rates of material removal rate under different grinding parameters were shown as in Figure 5.

Figure 5 shows that grinding parameters have various influences on the material removal rate. Grinding depth was the most important, followed by axial feed velocity, then wheel speed, and then workpiece speed. In order to validate the reliability of these models and the correctness of theoretical analysis, the following relevant experiments were carried out.

3. U-ELID Grinding Experiments

3.1. Equipment and Method. Experiments were carried out on a modified CNC machine center assisted with self-designed ultrasound and ELID devices. In order to make the results more comparable, the experiment used the contrastive analysis method, and the absence or presence of ultrasound and ELID devices was used to control the experiment state, as shown in Table 2, and the experimental setup was shown in Figure 6.

Workpieces were held in place on the working table and revolved under the rotating abrasive wheel, as shown in Figure 6(a). Before experiments were conducted, the workpieces were precisely manufactured to ensure that they had the same inner diameter. Each experiment was performed on each parameter group and repeated ten times, and the average value of the ten groups of experimental data was the final result. Before and after experiments, workpieces were washed with acetone and dried in a drier for about 30 minutes, and then the quality of workpiece was weighed with a precision electronic balance, as shown in Figure 6(b). The experimental conditions were described in detail in Table 3.

3.2. Results and Discussion. Under experimental conditions, grinding depth was greater than the critical ductile depth because it was 7 μm in most experiments, so the theoretical analysis in the case of $a_p < a_{pc}$ can be ignored. Figures 7 and 8 show the comparison between the theoretic analysis and experimental result after data processing.

From Figures 7 and 8, the material removal rate increases as the grinding parameters increase. Grinding depth has the greatest impact, followed by axial feed velocity, then wheel speed, and then workpiece speed. In addition, the change of material removal rate with the increase of grinding depth was shown in Figure 7, and there is a prominent change in the range of 3~5 μm, whether in theoretical or experimental results. This may be because the critical ductile depth is about 3.73 μm according the computational result in Section 2; the manner of material removal may transform from ductile to fracture in that range. Although the experimental data basically coincides with the theoretical analysis either in material removal rate or in parameter sensitivity, there is clear difference between them. This is because, to simplify the analysis, the theory analysis was merely to scratch the larger factors and ignore these less important factors. Moreover, these larger factors were described by mathematical formulas, which cannot fully express all the characteristics of these factors. So the theoretical analysis was just at the ideal state, and it cannot completely represent the realistic situations. But it captures the main contradiction, and we can have a deeper understanding of the U-ELID machining process and a guiding significance for the actual processing by the theoretical analysis. To examine the accuracy of the analysis, at the same time, the surface roughness was measured under different grinding depths by the White-Light Interferometry profilometer, and the machined surface was shown in Figure 9.

Figure 9 shows that when grinding depth was less than 3 μm, although there were some micro concavoconvex features and clear grinding traces on the machined surface, the overall surface quality was fairly good, so it can be concluded that the manner of material removal was dominated by the ductile mode at this point. Along with grinding depth increases, plowing ridges and grain traces weaken, and the workpiece surface becomes matte. This situation gradually intensifies, especially when the grinding depth was 7 μm; the surface quality decreases prominently, and

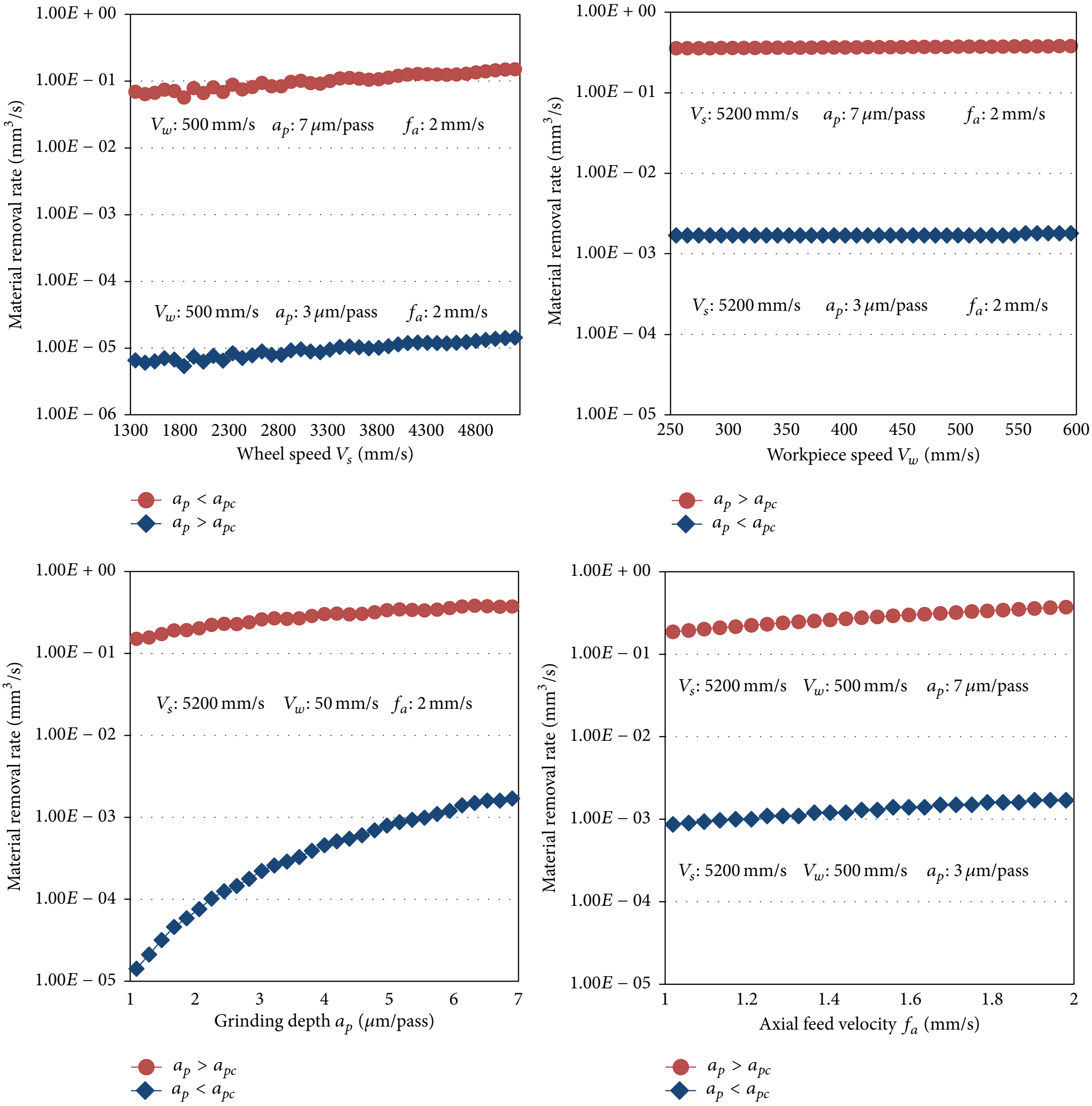

FIGURE 4: Comparison of theoretical analysis for material removal rate under grinding parameters.

the tiny broken particles and the scaly traces can be seen starkly on the machined surfaces. Therefore, the material removal method was brittle fracture mode at this time. Based on above experimental analysis, it can be predicted that the critical ductile depth must be in the range of 3~ 5 μm, which was just coinciding with the calculated results in Section 2. In order to make the results of evaluation more comparable, the surface roughness, under different grinding depths in different machining processes including ELID grinding (ELID), ultrasonic vibration-aided grinding (U), and U-ELID grinding (U-ELID), was measured and shown in Figure 10.

Figure 10 shows that in the U-ELID grinding the average height of the profile (R_a) and the point height of irregularities (R_z) were obviously lower than those in ELID grinding, but there was little difference compared with the ultrasonic vibration-aided grinding. This may be because the ultrasound produced the softening effect [17], and workpiece hardness decreases to some degree, while the electrolytic in-process dressing had less effect. So, the critical depth increases, and the machined quality was greatly improved. Moreover, the U-ELID grinding was proved to be an efficient method of ductile machining for nanocomposite ceramics, compared with ELID grinding and ultrasonic vibration-aided grinding.

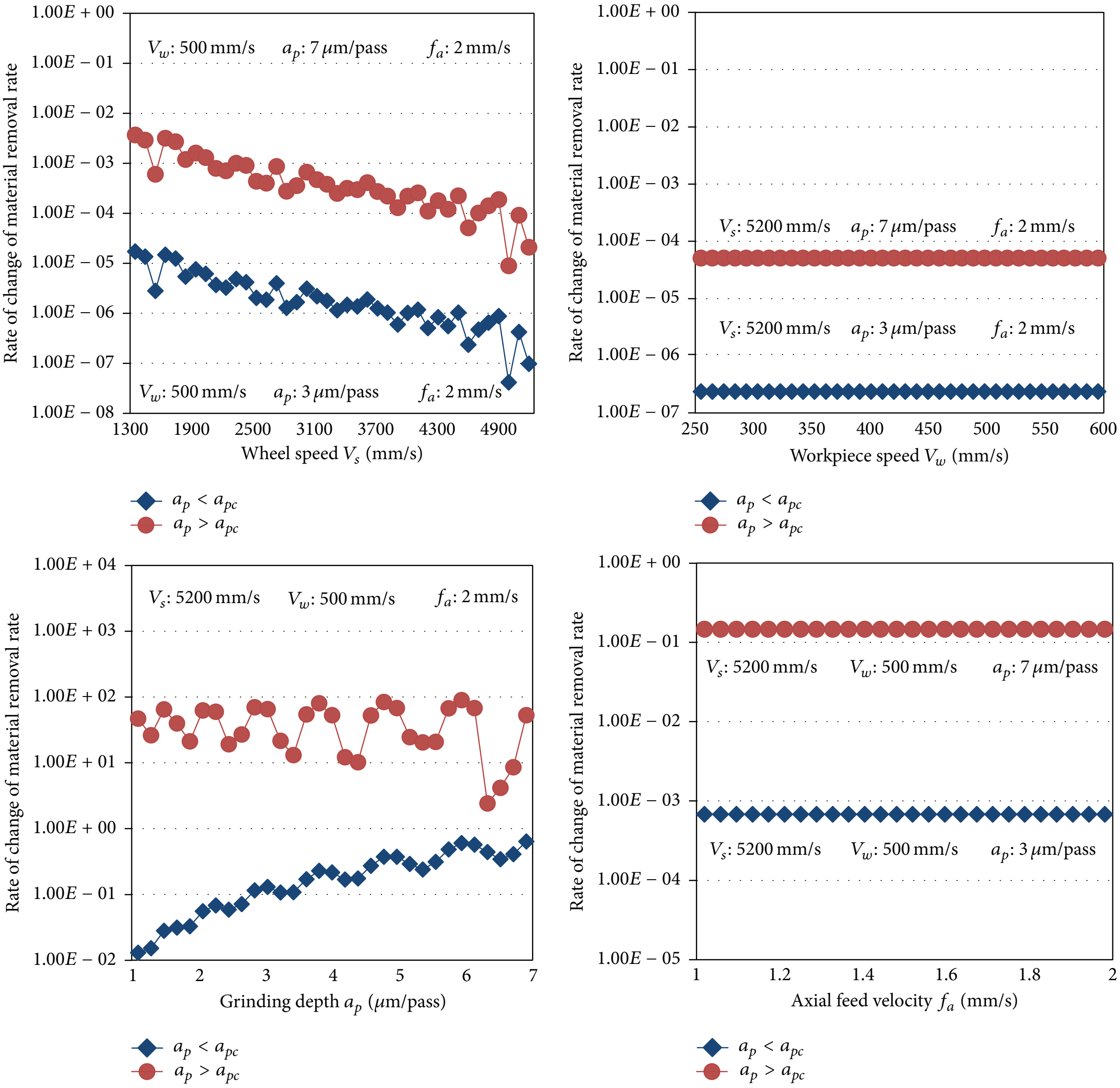

Figure 5: Comparison of theoretical analysis for parameter sensitivity under grinding parameters.

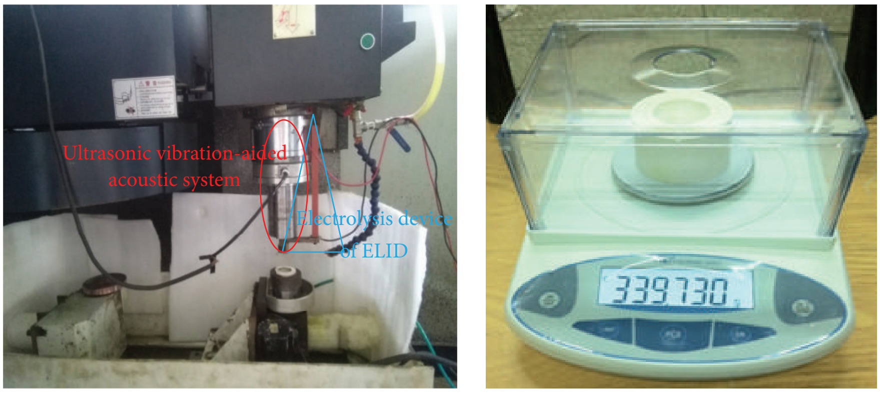

(a) Experimental setup

(b) Measuring equipment

Figure 6: Experimental setup.

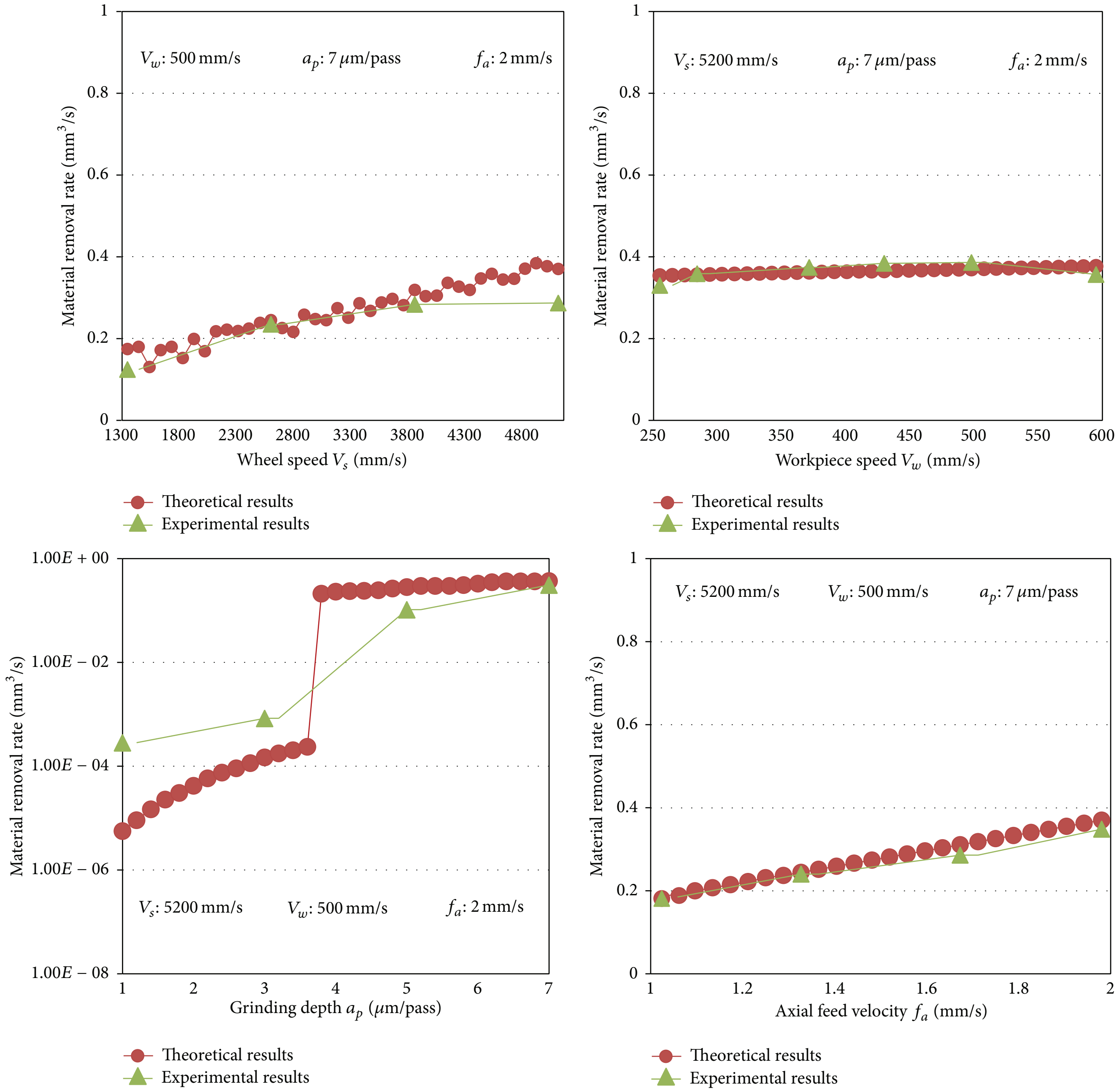

Figure 7: Comparison of theoretical and experimental analysis for material removal rate under grinding parameters.

4. Conclusions

In this study, some new formulas including material removal rate and sensitivity models of material removal rates on grinding parameter had been proposed, calculated, and experimented in U-ELID grinding, compared with ELID grinding and ultrasonic vibration-aided grinding. From this study the following conclusions can be drawn:

(1) The U-ELID grinding was analyzed to create mathematic models for material removal rate and parameter sensitivity, which were proved reliably and have greater significance for further optimizing other parameters.

(2) The removal rate increases as the grinding parameters increase. In order, the most important parameters were grinding depth, axial feed velocity, wheel speed, and workpiece speed. Considering the machining surface quality, the optimal comprehensive performance was obtained when grinding depth (key parameter) was about 3.73 μm.

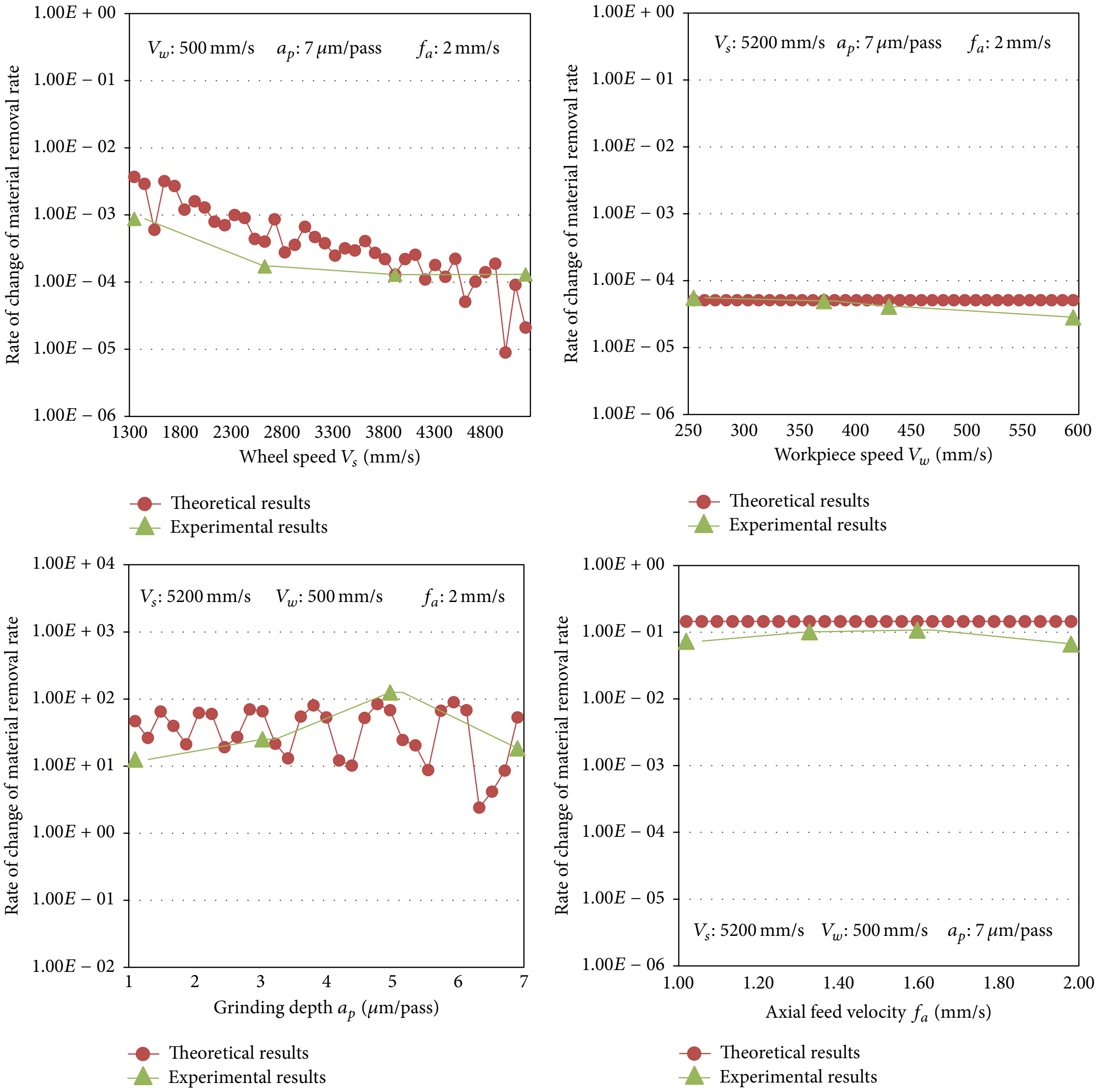

FIGURE 8: Comparison of theoretical and experimental analysis for parameter sensitivity under grinding parameters.

(3) The U-ELID grinding has a wider efficient ductile machining range which makes it a highly efficiency, ultra-precise mirror processing technology for nanocomposite ceramics, compared with ELID grinding and ultrasonic vibration-aided grinding.

Nomenclature

A: Amplitude of ultrasonic vibration (μm)
A_a: Effective conducting area on anode (mm^2)
a: Feature size on indentation (mm)
a_p: Grinding depth (mm)
a_p': Actual grinding depth (mm)
a_{pc}: Nominal critical grinding depth (mm)
a_{pc}': Actual critical grinding depth (mm)
C_g: Constant caused by dynamic performance of wheel
C_h: Depth of transversal crack (mm)
C_L: Length of transversal crack (mm)
C_s: Static effective grains' number per unit area (/mm^2)
d_{se}: Equivalent diameter of wheel (mm)
F: Faraday's constant
f: Frequency of ultrasonic vibration (Hz)

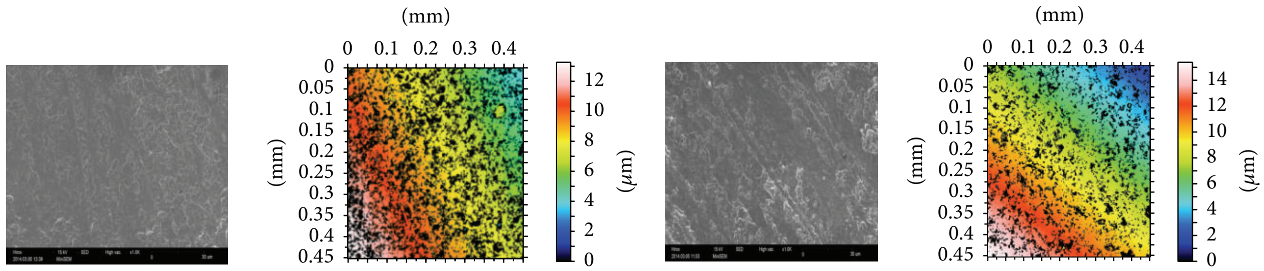

(a) 1 μm (b) 3 μm

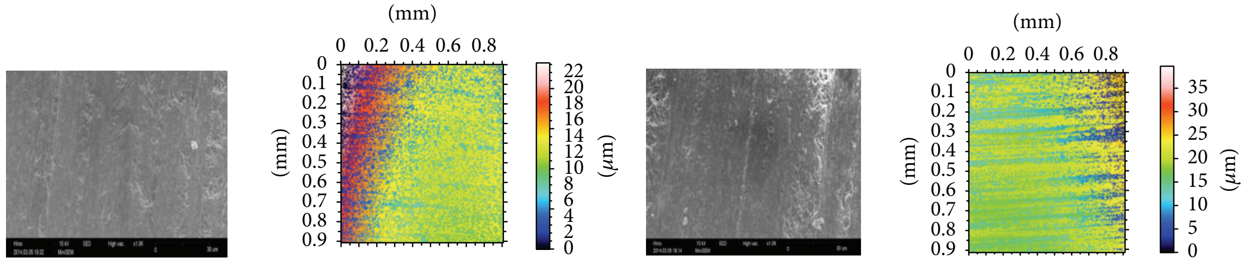

(c) 5 μm (d) 7 μm

Figure 9: Surface topography under different grinding depths.

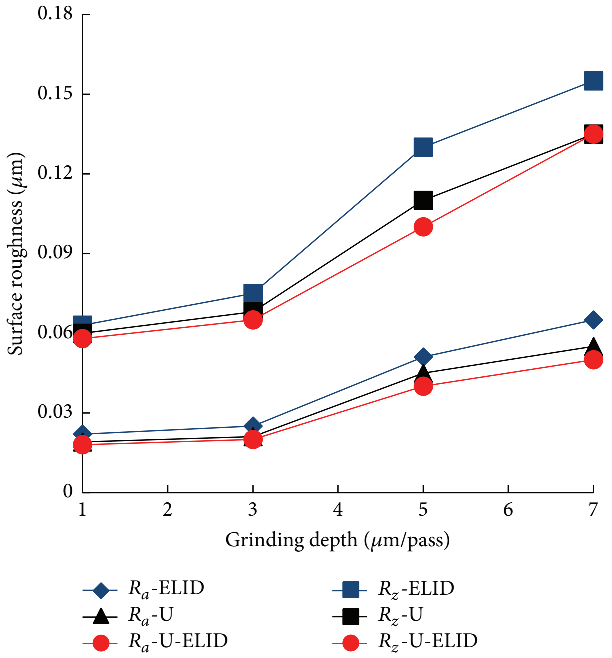

Figure 10: Surface roughness under different grinding depths.

Table 1: Relevant parameters.

Objects	Parameters	Value
Workpiece	Material	Nano-zirconia toughened alumina nanocomposite ceramic
	Density (ρ)	4.9 g/cm^3
	Fracture toughness (K_{IC})	7.9 Mpa·m$^{1/2}$
	Vickers hardness (H_v)	10.9 Gpa
	Elasticity modulus	315 Gpa
	Poisson's ratio	0.3
	Average grain size	50 nm
	Inner diameter (d_w)	35 mm
Wheel	Material	Cast iron bond diamond wheel
	Concentration	100%
	Model	W40
	Outer diameter (d_s)	Φ25 mm
	Width	17 mm
	Half taper angle (θ)	60°
Grinding parameters	Wheel speed (V_s)	1.3 m/s–5.2 m/s
	Workpiece speed (V_w)	0.28 m/s–0.5 m/s
	Axial feed velocity (f_a)	1 mm/s-2 mm/s
	Grinding depth (a_p)	1 μm/pass–7 μm/pass
	Ultrasonic frequency (f)	35000 Hz
	Ultrasonic amplitude (A)	10 μm

f_a: Axial feed velocity of wheel (mm/s)
H_v: Hardness of workpiece (Pa)
h_d: Thickness of oxidation film (mm)
I: Current of electrolysis (A)
K_{IC}: Fracture toughness of workpiece (Pa·mm)
K_m: Impact coefficient of ultrasonic vibration on movement state

Table 2: Experiment methods.

Experiment state	Ultrasonic generator	Special power source of ELID
U-ELID grinding	Open	Open
ELID grinding	Close	Open
Ultrasonic grinding	Open	Close

Table 3: Conditions of experiment.

Parameters	Conditions
Wheel truing	Voltage: 120 V; duty ratio: 5 μs : 5 μs; wheel speed: 1000 r/min
Wheel sharpening	Truing wheel speed: 1000 r/min; voltage: 120 V; duty ratio: 5 μs : 5 μs; electrode gap: 1 mm; wheel speed: 1000 r/min
Workpieces	Nano-zirconia toughened alumina nanocomposite ceramic, outer diameter: Φ60 mm, inner diameter: Φ35 mm, height: 40 mm
Diamond wheel	Diameter: 25 mm, height: 17 mm, particle size: 280#, cast iron bond, concentration: 100%
Wheel speed	1.3 m/s, 2.6 m/s, 3.9 m/s, 5.2 m/s
Workpiece speed	0.28 m/s, 0.37 m/s, 0.43 m/s, 0.5 m/s
Axial feed velocity	60 mm/min, 80 mm/min, 100 mm/min, 120 mm/min
Grinding depth	1 μm/pass, 3 μm/pass, 5 μm/pass, 7 μm/pass
Grinding fluids	Ratio of mother liquor to distilled water: 1 : 50
Special power supply voltage	90 V
Duty ratio	5 μs : 5 μs
Interelectrode gap	0.3 mm
Ultrasonic parameters	Frequency: 34.835 kHz, amplitude: 10 μm

"#" is the grain size unit of Japan.

K_d: Impact coefficient of dynamic parameters on dynamic fracture toughness

M: Molecular weight of metal bond (g/mol)

N_d: Dynamic effective grains

P: External load (N)

P_c: Critical load (N)

R: Total resistance in ELID circuit (Ω)

S: Cross-sectional area (mm^2)

t: Valid time of electrolysis (s)

U: Electrode voltage (V)

V: Relative velocity between wheel and work piece (mm/s)

V_w: Linear velocity of work piece (mm/s)

V_s: Linear velocity of wheel (mm/s)

V_v: Electrolyte content (mm^3)

z: Valence of metallic element

ξ: Geometrical factor of diamond indenter

η: Current efficiency

θ: Half-angle of indenter or grain (rad)

λ_0: Correlation coefficient

ρ: Density of metal bond (g/mol)

φ: Initial angle of ultrasonic vibration (rad)

ω: Angular velocity (rad/s).

Competing Interests

The authors declare that there is no conflict of interests regarding the publication of this paper.

Acknowledgments

The authors sincerely acknowledge the National Science Foundation of China (Contract nos. 51175153 and 51475148) and the Fostering Foundation of Henan Polytechnic University for the Excellent Ph.D. Dissertation, for their financial support of this research project.

References

[1] S.-D. Yoon, H.-S. Byun, and Y.-H. Yun, "Characterization and photocatalytic properties of ceramics TiO_2 nanocomposites," *Ceramics International*, vol. 41, no. 6, pp. 8241–8246, 2015.

[2] C. M. Zhang, "Study of small cracks on nanocomposite ceramics cut by WEDM," *International Journal of Advanced Manufacturing Technology*, vol. 83, no. 1–4, pp. 187–192, 2016.

[3] M. L. Wu, K. F. Zhang, and C. Z. Ren, "Study on the non-uniform contact during ELID groove grinding," *Precision Engineering*, vol. 39, pp. 116–124, 2015.

[4] Q. L. Zhao and B. Guo, "Ultra-precision grinding of optical glasses using mono-layer nickel electroplated coarse-grained diamond wheels. Part 1: ELID assisted precision conditioning of grinding wheels," *Precision Engineering*, vol. 39, pp. 56–66, 2015.

[5] J. Murata, Y. Ueno, K. Yodogawa, and T. Sugiura, "Polymer/CeO_2–Fe_3O_4 multicomponent core-shell particles for high-efficiency magnetic-field-assisted polishing processes," *International Journal of Machine Tools & Manufacture*, vol. 101, pp. 28–34, 2016.

[6] K. Egashira, R. Kumagai, R. Okina, K. Yamaguchi, and M. Ota, "Drilling of microholes down to 10 μm in diameter using ultrasonic grinding," *Precision Engineering*, vol. 38, no. 3, pp. 605–610, 2014.

[7] A. Zahedi, T. Tawakoli, and J. Akbari, "Energy aspects and workpiece surface characteristics in ultrasonic-assisted cylindrical grinding of alumina-zirconia ceramics," *International Journal of Machine Tools & Manufacture*, vol. 90, pp. 16–28, 2015.

[8] F. Chen, B. Zhao, X. F. Jia, and X. B. Wang, "Material removal rate for nanocomposite ceramics in ultrasound-aided electrolytic in process dressing," *Proceedings of the Institution of Mechanical Engineers Part C: Journal of Mechanical Engineering Science*, 2016.

[9] M. K. Gupta, P. Sood, and V. S. Sharma, "Optimization of machining parameters and cutting fluids during nano-fluid based minimum quantity lubrication turning of titanium alloy

by using evolutionary techniques," *Journal of Cleaner Production*, vol. 135, pp. 1276–1288, 2016.

[10] L. Selvarajan, C. Sathiya Narayanan, R. Jeyapaul, and M. Manohar, "Optimization of EDM process parameters in machining $Si_3N4\text{-}TiN_4$ conductive ceramic composites to improve form and orientation tolerances," *Measurement*, vol. 92, no. 1, pp. 114–129, 2016.

[11] M. V. Swain and B. R. Lawn, "Indentation fracture in brittle rocks and glasses," *International Journal of Rock Mechanics and Mining Sciences & Geomechanics Abstracts*, vol. 13, no. 11, pp. 311–319, 1976.

[12] T. G. Bifano, T. A. Dow, and R. O. Scattergood, "Ductile-regime grinding: a new technology for machining brittle materials," *Journal of Engineering for Industry*, vol. 113, no. 2, pp. 184–189, 1991.

[13] T. R. Wilshaw, C. A. Rau, and A. S. Tetelman, "A general model to predict the elastic-plastic stress distribution and fracture strength of notched bars in plane strain bending," *Engineering Fracture Mechanics*, vol. 1, no. 1, pp. 197–211, 1968.

[14] D. J. Stephenson, X. Sun, and C. Zervos, "A study on ELID ultra precision grinding of optical glass with acoustic emission," *International Journal of Machine Tools and Manufacture*, vol. 46, no. 10, pp. 1053–1063, 2006.

[15] B. Kersschot, J. Qian, and D. Reynaerts, "The electrical behaviour of the dressing process in ELID-grinding," *International Journal of Nanomanufacturing*, vol. 9, no. 2, pp. 137–147, 2013.

[16] Z. J. Pei, P. M. Ferreira, and M. Haselkorn, "Plastic flow in rotary ultrasonic machining of ceramics," *Journal of Materials Processing Technology*, vol. 48, no. 1–4, pp. 771–777, 1995.

[17] G. S. Kelly, S. G. Advani, J. W. Gillespie Jr., and T. A. Bogetti, "A model to characterize acoustic softening during ultrasonic consolidation," *Journal of Materials Processing Technology*, vol. 213, no. 11, pp. 1835–1845, 2013.